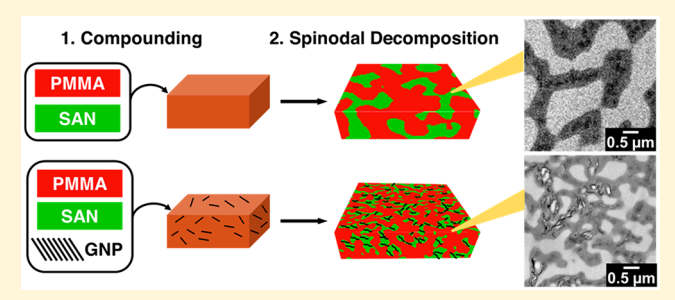
# Polymer/Graphene Composites via Spinodal Decomposition of Miscible Polymer Blends

Yangming Kou, Xiang Cheng, and Christopher W. Macosko

Department of Chemical Engineering and Materials Science, University of Minnesota, Minnesota, Minnesota 55455, United States

Supporting Information

**ABSTRACT:** Conductive polymer composites (CPCs) enjoy broad industrial applications such as electrostatic discharge (ESD) protection. Herein, we constructed CPCs by first solution blending graphene nanoplatelets (GNPs) into a miscible blend of poly(methyl methacrylate) (PMMA) and poly(styrene-co-acrylonitrile) (SAN) and then inducing PMMA/SAN spinodal decomposition by annealing well above the lower critical solution temperature. The resulting composite showed spatially regular, co-continuous polymer domains, in which GNPs preferentially localized within the SAN-rich phase and formed a conductive network. We found



that GNPs induced local nucleation of SAN into surface layers of  $\sim 4R_{\rm g}$  in thickness. Small PMMA domains formed next to these SAN layers and were stable against long annealing times. As a result, GNPs created local blend morphologies that were different from the bulk morphology arising from spinodal decomposition alone. During annealing, GNPs suppressed domain coarsening and preserved the co-continuous morphology, while their connectivity in the polymer matrix was improved. Additionally, inducing PMMA/SAN phase separation significantly increased the ternary blend's electrical conductivity by over 5 orders of magnitude. Compared to the conventional approach of CPC manufacture of compounding carbon black into a homopolymer matrix, our approach achieved bulk electrical conductivity of  $\sim 10^{-8}$  S/cm at 1 wt % GNP loading, rendering this system suitable for ESD protection.

## 1. INTRODUCTION

Conductive polymer composites (CPCs), polymer systems with high electrical conductivity, have broad industrial and technical applications and are projected to have a global market demand of over 7 billion USD by 2021. In general, CPCs with electrical conductivity from 10<sup>-11</sup> to 10<sup>-4</sup> S/cm are suitable for electrostatic discharge (ESD) protection (e.g., fuel component protection for automobiles and aircraft, packaging and storage for sensitive electronic devices, etc.), while those whose electrical conductivity range from 10<sup>-6</sup> to 10<sup>0</sup> S/cm are useful for electromagnetic interference (EMI) shielding (e.g., protection of electronic devices against passive interference).2-6 The traditional approach of producing CPCs for ESD protection is by melt compounding carbon black (CB) filler particles into a homopolymer matrix.<sup>7,8</sup> This approach requires the filler loading to be above the percolation threshold,9 which is the minimum filler loading required for a continuous conductive pathway to form throughout the composite. For CB particles, the effective filler loading required to achieve ESD protection-suitable conductivities was reported to be 15-30 wt % in poly(methyl methacrylate) (PMMA). 10-12 This leads to various challenges such as the higher cost of raw materials, increased melt viscosity, decreased processability, and particles sloughing from the final part, causing limitations on these composites' applications. Therefore, it is of significant research interest to develop strategies to reduce the filler loading to achieve conductive percolation in these polymer composites.

One strategy to reduce filler loading is by selecting conductive fillers with higher intrinsic conductivity and aspect ratio. In recent years, graphene nanoplatelets (GNPs) have emerged as attractive fillers for producing CPCs with lower filler loading. GNPs have two-dimensional structure with high aspect ratio, which promote the buildup of a conductive filler network as compared with spherical fillers such as carbon black.<sup>13</sup> They also have high intrinsic electrical conductivity (106 S/cm for pure graphene), in addition to having high mechanical stiffness and strength, which favors their incorporation to producing CPCs with superior properties. Stankovich et al. reported the first attempt in producing graphene-based polymer composites by compounding reduced graphene oxide sheets in a polystyrene matrix.<sup>14</sup> These composites achieved electrical conductivity of 10<sup>-8</sup> S/cm at 0.15 vol % (~0.33 wt %) loading, which was slightly above the estimated percolation threshold of 0.1 vol % (~0.22 wt %). Past work from our group has also reported the estimated conductivity percolation of functionalized graphite sheets (~8 layers of stacked graphene sheets) was 0.3 vol %. 15 However, because of the higher cost of

Received: July 4, 2019 Revised: September 12, 2019 Published: October 2, 2019

GNPs as compared to CB particles, it is desirable to design the polymer matrix to further reduce the filler loading to achieve favorable electrical conductivities in these composites.

Another strategy to reduce filler loading is to use an inhomogeneous polymer blend instead of a homopolymer matrix. This is most commonly achieved by using an immiscible, co-continuous polymer blend. Then, the percolation threshold may be further reduced by achieving double percolation, i.e., selective localization of the conductive fillers in either one continuous phase or more preferably at the interface. Selective localization of conductive fillers such as CB, 16,17 carbon nanotubes, 18,19 and graphene 20 into an immiscible co-continuous phase has been found to reduce the percolation threshold required as compared to compounding into a homopolymer matrix by approximately 2-4-fold. However, immiscible blends are not at equilibrium as they undergo continuous coarsening during processing. Preventing coarsening and preserving the double percolated morphology are both crucial for maintaining the high electrical conductivity and mechanical integrity of these composites for practical applications. Thus, immiscible blend pairs need to be carefully selected based on their melt viscosity, interfacial tension, and processing parameters such as temperature and annealing time. On the other hand, interfacially localized filler particles can more significantly reduce the percolation threshold by over 10fold as compared to compounding into a homopolymer matrix. 16 Interfacial localization can be achieved by using neutrally wetting particles that stabilize at the immiscible blend interface. We have previously demonstrated this by compounding functionalized silica particles into polystyrene (PS)/ PMMA blends.<sup>21</sup> However, surface functionalization of carbon-based conductive fillers is typically difficult as well as expensive and usually reduces their intrinsic conductivity. Another option is to use a two-step melt compounding sequence: the conductive fillers are first compounded into the thermodynamically unfavored polymer and then compounded a second time with the thermodynamically favored polymer. During the second compounding process, the fillers will transfer to the favorable, phase but a fraction of them will become kinetically trapped at the interface. 22-24 Nonetheless, this approach requires additional processing steps and proper control of the processing parameters to prevent insufficient migration or particle detachment from the interface during melt compounding, which may limit the practical applications

An alternative of using immiscible polymer blends to construct co-continuous morphologies is by the spinodal decomposition of miscible polymer blends. By heating an initially homogeneous, near-critical polymer blend inside the spinodal curve, the polymer blend spontaneously phase separates into finely dispersed, co-continuous domains. These structures exhibit self-similar coarsening behavior during annealing, which preserves their co-continuous morphology over longer periods of time. Many previous efforts have been made in using filler particles to construct and maintain nonequilibrium morphologies arising from spinodal decomposition. For example, by placing neutrally wetting silica particles in miscible liquids, the co-continuous morphology formed by spinodal decomposition can be preserved because the particles jam at the interface and suppress domain coarsening. This leads to the creation of a class of materials known as the bicontinuous interfacially jammed emulsion gels (bijels) by using either polar<sup>25</sup> or nonpolar<sup>26</sup> liquid pairs. Similarly, interfacial localization of silica particles with PS chains grafted at the surface has been achieved upon spinodal decomposition of PMMA/poly(styrene-co-acrylonitrile) (SAN) systems.<sup>27</sup> However, the extreme challenge that fillers must exhibit neutral wetting for interfacial localization still remains. Therefore, without filler surface chemistry modification, the expected morphology upon phase separation is selective filler percolation within one phase. Li and co-workers demonstrated that adding 2 vol % (~11.5 wt %) CdSe nanorods can arrest the spinodal decomposition of lowmolecular-weight PS/poly(vinyl methyl ether) (PVME) polymer blends, as the nanorods selectively percolate within the PVME phase and cause intraphase gelation.<sup>28</sup> Filler particles can affect the phase separation and coarsening dynamics of miscible polymer pairs over a large composition range. As a result, prior efforts were made by loading conductive multiwall carbon nanotube (MWCNT)<sup>29</sup> and thermally reduced graphene sheet (TRG)<sup>30</sup> filler particles into off-critical blends of PMMA/poly[( $\alpha$ -methylstyrene)-coacrylonitrile] (P $\alpha$ MSAN) miscible blends. Upon phase separation of PMMA/PaMSAN, the conductive fillers, which thermodynamically favor the PaMSAN phase, induced nucleation of PaMSAN to form interconnected filler-rich domains. Additionally, when filler loading was above a critical volume fraction, they further act as physical barriers to effectively suppress coalescence of the droplet-matrix morphology. Consequentially, biphasic polymer composites formed by phase separation had higher electrical conductivity than homopolymer composites of the same filler loading.

Herein, we report a method to construct CPCs using a PMMA/SAN/GNP ternary blend. Commercially available GNPs were specifically chosen due to their high electrical conductivity and high aspect ratio, both of which favor conductive percolation at low loading levels. The PMMA/SAN blend was selected as the polymer pair, as their partial miscibility characterized by a lower critical solution temperature (LCST) phase behavior has been widely studied and understood: SAN with ~30 wt % acrylonitrile and PMMA have reported LCST values of ~175  $\pm$  10 °C,  $^{27,31-33}$  which falls in the range of the processing temperatures for both polymers. In addition, these polymers are also commercially available and have robust mechanical properties. In this paper, we first use a combination of optical cloud point measurements, rheology, and transmission electron microscopy (TEM) to construct the phase diagram of PMMA/SAN blends. We then construct CPCs by spinodal decomposition and subsequent annealing of PMMA/SAN/GNP ternary blends. Our results show that GNPs localize and percolate entirely within the SAN-rich phases upon spinodal decomposition, resulting in blends with room temperature bulk dc conductivity of  $\sim 10^{-8} - 10^{-10}$  S/cm at 1 wt % ( $\sim 0.45$  vol %) GNP loading. Our work further systematically characterizes the blend morphology before and after phase separation via TEM. Using quantitative image analyses, rheology, and time-resolved electrical conductivity measurements, we elucidate the effect of GNP fillers on the kinetics of domain coarsening and the resultant bulk and local morphology. As compared to immiscible polymer pairs, our approach involves fewer processing steps to produce finely dispersed and spatially regular co-continuous blend morphology to result in CPCs with low GNP loading suitable for ESD protection applications. Our study also demonstrates the influence of conductive fillers on the phase dynamics of miscible polymer

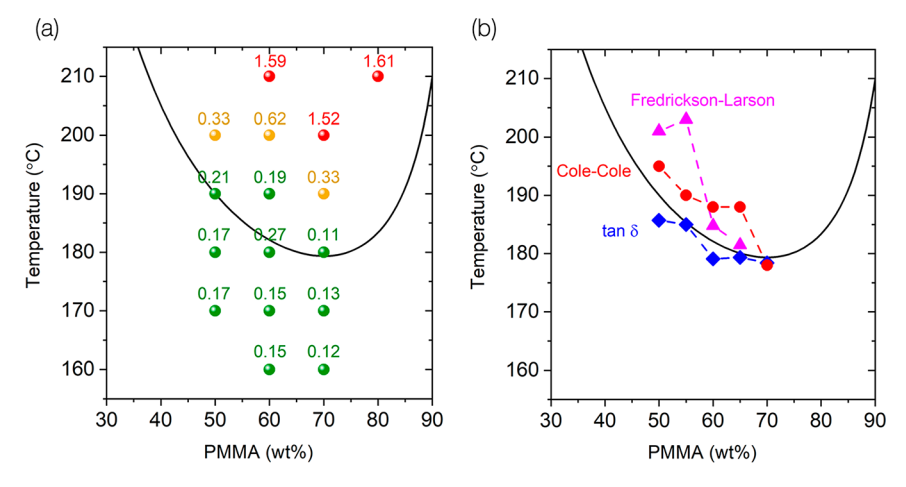


Figure 1. Phase diagram of PMMA/SAN blends obtained by using (a) cloud point measurements and (b) shear rheology. In (a), results are given as optical attenuation ( $\mu$ ), which is the optical absorbance normalized with sample thickness. Each data point is color-coded to represent their appearances by the naked eye: opaque (red;  $\mu$  > 1.0 A/mm), intermediate (yellow; 0.3 <  $\mu$  < 1.0 A/mm), and transparent (green;  $\mu$  < 0.3 A/mm). In (b), the phase diagrams are obtained from tan  $\delta$ , Cole—Cole, and Fredrickson—Larson plots. In both figures, the solid lines show the calculated spinodal lines from the Flory—Huggins theory<sup>31,32</sup> (see the Supporting Information, section S2.2).

blends, which we hope can guide toward better future design of these functional CPCs.

## 2. EXPERIMENTAL SECTION

**2.1. Preparation of PMMA/SAN/GNP Composites.** 2.1.1. Materials. PMMA ( $M_{\rm w}=36.0~{\rm kg/mol}$ , D=1.81,  $\rho=1.18~{\rm g/cm^3}$ ) and SAN (30 wt % acrylonitrile,  $M_{\rm w}=155.4~{\rm kg/mol}$ , D=2.12,  $\rho=1.08~{\rm g/cm^3}$ ) powders were obtained from Fisher Scientific and Sigma-Aldrich, respectively, and used as received. Molecular weight distributions were measured using size-exclusion chromatography (Supporting Information, section S1). GNPs (N002-PDR,  $\rho=2.2~{\rm g/cm^3}$ , specific surface area =  $400-500~{\rm m^2/g}$ ) were purchased from Angstron Materials. According to the manufacturer, the GNPs have  $\geq 95.00~{\rm wt}$  % carbon and  $\leq 2.50~{\rm wt}$  % oxygen content. The average lateral dimension of GNPs was  $\leq 10~{\mu}{\rm m}$ , and thickness was  $\sim 1.0-1.2~{\rm nm}$ , corresponding to an average three-layer stack of graphene sheets.  $^{34}$  Particle size distribution in the 10th, 50th, and 90th percentile were reported to be 4.5-6.0, 8.0-9.5, and  $11.0-18.0~{\mu}{\rm m}$ , respectively (Microtrac Particle Analysis).

2.1.2. Composite Preparation. Both the binary PMMA/SAN neat blends and the ternary PMMA/SAN/GNP blends were compounded below the LCST. The notation "xx/yy/zz" is used to denote compositions, where "xx/yy" represents the weight ratio between PMMA/SAN and "zz" represents the weight percent of GNP filler relative to the weight of polymers. The PMMA/SAN neat blends were prepared by using a conical twin-screw microcompounder (Xplore MC5) under N2 protection. PMMA and SAN powders were added to the microcompounder at 50 rpm within 1 min at 170 °C and then mixed for 5 min. The extruded material was quenched into liquid nitrogen. Miscible PMMA/SAN blends appeared transparent with a slight yellow tint, which is attributed to the partial cyclization of polyacrylonitrile units within SAN. 35,36 PMMA/SAN/GNP ternary blends were prepared via solvent blending. We dispersed GNP flakes into tetrahydrofuran (THF, reagent grade, Sigma-Aldrich) at a concentration of 1 mg/mL to obtain 40 mL of GNP/THF suspension. The suspension was probe sonicated (Branson Digital Sonifier SFX 250) continuously at 75 W for 1 h under an ice water bath. In a separate container, a total of 4 g of polymer powders was dissolved in 40 mL of THF. The polymer solution was combined with the sonicated GNP/THF suspension under continuous stirring for 10 min before coprecipitation into ~1 L of methanol. The resulting precipitate was filtered, dried in vacuo at 60 °C overnight, and compression molded at 170 °C into circular disks, 25 mm in diameter and ~1 mm in thickness, for subsequent characterization.

2.1.3. Annealing. Polymer blend samples were annealed under nitrogen flow using the convection oven of an ARES rheometer (TA Instruments). Each sample was first sandwiched between two pieces of Teflon-coated fiberglass fabric and then gently compressed by using the 25 mm parallel plate geometry fixtures at prescribed temperatures. Upon the end of annealing, the sample was submerged into a room temperature water bath to "freeze" the morphology.

**2.2. Characterization.** 2.2.1. Cloud Point Measurement. We determined cloud point temperatures by measuring light transmittance through the PMMA/SAN neat blend samples after annealing at various temperatures. Samples were compression molded into disks of thickness 0.8 mm at 160–210 °C for 10 min, before quenching to room temperature in a cold water bath. The sample turbidity was measured by shining a red laser through each sample into a Si photodiode (Thorlabs, FDS010) at room temperature.

2.2.2. Shear Rheology. We measured the PMMA/SAN samples' dynamic rheological characteristics with an ARES rheometer using 25 mm diameter parallel plates under nitrogen. The composition of PMMA/SAN blends used in rheological measurements were from 50/50 to 70/30, as they were expected to produce co-continuous morphologies, and these ratios were close to the critical composition reported in the literature.  $^{31,32}$  We performed dynamic temperature ramp tests from 150 to 230 °C with heating ramp rate of  $\leq$ 1 °C/min at a frequency of 0.03 rad/s and isothermal dynamic frequency sweep tests from 100 to 0.063 rad/s at a series of temperatures in proximity to the spinodal temperature. Dynamic strain sweeps were taken for each sample to ensure the maximum applied strain amplitude produced sufficiently large torque signals while maintaining the applied deformation in the linear viscoelastic regime.

2.2.3. TEM Microscopy. Polymer blends were sectioned using a Leica EM UC6 ultramicrotome with a diamond knife at room temperature to nominal thicknesses of ~60 nm. Ultrathin sections were transferred onto copper mesh grids using an eyelash (Ted Pella). Bright-field TEM images were obtained using a FEI Tecnai T12 or FEI Tecnai G2 Spirit BioTWIN microscope, both of which were operated at an accelerating voltage of 120 kV and were equipped with a CCD camera.

2.2.4. Electrical Conductivity. We measured the bulk dc conductivity of the PMMA/SAN/GNP blends at room temperature using a two-probe method. Compression molded samples,  $\sim 1$  mm thick, were placed on a gold-coated silica wafer. Then, the sample surface and the conductive wafer were contacted with the test electrode. The current response of the sample was measured in the out-of-plane direction of the composites by performing I-V sweep by applying a dc potential bias of  $\pm 20$  V between the two probes at 1 V/s

sweeping rate. Each value was an average of at least three measurements.

We also simultaneously measured viscoelastic and dielectric characteristics on an ARES rheometer using a 25 mm parallel plate geometry equipped with the TA Instruments dielectric accessory at 200 °C for 2 h. This allowed us to monitor the evolution of rheology and electrical conductivity that occurred during phase separation and annealing. The experimental setup was similar to that of Bai et al.<sup>2</sup> PMMA/SAN/GNP samples were initially prepared by room temperature solvent blending such that the polymers were miscible. Then, the samples were placed in the preheated rheometer oven at 200 °C for at least 5 min to equilibrate sample temperature and induce PMMA/SAN phase separation. We measured the dynamic moduli at 2-7% strain with 0.1 rad/s in the linear viscoelastic regime. The dielectric accessory supplied a constant rms electric potential of 1 V with an ac frequency  $\omega_{ac}$  between 20 Hz and 1 GHz across the sample. This allowed measurement of the samples' complex capacitance, C\*, which relates to the samples' complex electrical permittivity and electrical conductivity as

$$\varepsilon^* = \varepsilon' - i\varepsilon'' = \frac{C^*d}{\varepsilon_0 A} \tag{1}$$

$$\sigma^* = \sigma' + i\sigma'' = \omega_{ac} \varepsilon_0 \varepsilon'' + i\omega_{ac} \varepsilon_0 \varepsilon'$$
 (2)

where  $\varepsilon_0$  represents the permittivity in a vacuum, A the sample area, and d the sample thickness. In the limit of low  $\omega_{ac}$ , the real part of the complex conductivity approaches the dc electrical conductivity (Figure S9).

## 3. RESULTS AND DISCUSSION

**3.1. Construction of the Phase Diagram.** The LCST behavior of the PMMA/SAN system was verified by performing cloud point and shear rheology measurements. Two types of rheological measurements, namely, dynamic temperature sweep and a series of isothermal dynamic frequency sweep experiments, were used to detect the onset of PMMA/SAN phase separation. The dynamic temperature sweep data were used to construct tan  $\delta$  and Fredrickson–Larson plots, while the isothermal dynamic frequency sweep data were used to construct Cole–Cole plots. The resulting PMMA/SAN phase diagram is given in Figure 1 and Table 1; more experimental details and analysis are provided in the Supporting Information, section S2.

Table 1. Phase Separation Temperature (in °C) of PMMA/SAN Neat Blends As Determined by Cloud Point, Rheology, and Flory–Huggins Theory<sup>31,32</sup>

PMMA/SAN (wt %)	cloud point	tan $\delta$	Fredrickson— Larson	Cole– Cole	Flory– Huggins
50/50	195	186	201	195	190
55/45		185	203	190	185
60/40	195	179	185	188	182
65/35		179	182	188	180
70/30	185	178		178	179

Both our cloud point and rheology measurements qualitatively agree with the calculated spinodal curve (Figure 1). The critical composition likely occurs at 70/30 wt % PMMA/SAN with critical temperature  $T_{\rm s}\sim 178$  °C, which agrees with the blend morphology from TEM images (see below). The rheology methods provided more precision than the cloud point measurements. Both tan  $\delta$  and Cole—Cole plot methods provided  $T_{\rm s}$  values matching closely to the calculated spinodal curve.  $T_{\rm s}$  obtained from the Fredrickson—Larson plot showed a deviation of up to ~20 °C from the theoretical value.

Similar deviations have been observed when using the Fredrickson–Larson plots to detect  $T_{\rm s}$  in a number of previous works.  $^{30,33,37}$  The source of error has been attributed to the breakdown of the mean-field assumption that G' of the miscible blend was dominated by concentration fluctuation for polymer blend systems.  $^{33}$  The theory also neglects factors such as segmental chain motion, intramolecular entanglements,  $^{37}$  and polymer polydispersity, which could further increase the error. We provide more discussion in the Supporting Information, section S2.2.

The phase diagram of PMMA/SAN/GNP ternary blends has not been systematically probed. But we do expect that the addition of GNP fillers will lower the LCST between PMMA and SAN. Vleminckx et al. reported that loading TRG sheets, whose sheet dimensions were similar to GNPs in this work, led to an ~9 °C decrease of LCST in a similar blend of PMMA/ PαMSAN.<sup>30</sup> The finding is consistent with the Ginzburg model,<sup>38</sup> which predicts the decrease of the LCST for filler particles significantly larger than the polymer coils. We observed the emergence of a surface layer of SAN chains adsorbed around GNPs, which occurs within the first 5 min of annealing above the LCST (see TEM results below). The SAN surface layers can effectively act as nucleation sites to induce polymer phase separation at a lower temperature, leading to the local lowering of the LCST. The emergence of such surface layer around filler particles has also been observed in PMMA/ SAN/silica particle systems, <sup>39,40</sup> in which the critical temperature around the surface layer was measured to be lower than that of the bulk polymer matrix.4

For the above reasons, the ternary PMMA/SAN/GNP blends were prepared by solution blending at room temperature, which is well below the neat blend LCST, to ensure PMMA and SAN were initially mixed into a homogeneous state prior to inducing phase separation.

3.2. Effect of GNP Fillers on the Phase-Separated Blend Morphology. In addition to cloud point and rheology measurements, TEM images further confirmed that annealing at 200 °C results in phase separation between PMMA and SAN. Figure 2 shows representative blend morphologies for both 70/30 PMMA/SAN neat blends (column A) and 70/30/ 1 PMMA/SAN/GNP ternary blends (column B), before and after phase separation. Blends that were prepared below the LCST showed clear miscibility in TEM images (Figure 2, row 1), in which PMMA and SAN chains exhibited a uniform electron density across the entire sample except for black spots ~100 nm in diameter throughout the field of view. Upon annealing at 200 °C (Figure 2, rows 2-6), PMMA/SAN spinodally decomposed into co-continuous, phase-separated domains. No staining was necessary in obtaining these images: Thomas et al. studied the same system and found that the PMMA-rich regions were subject to mass loss and preferential thinning under electron beam irradiation due to chain scission. 41 On the other hand, SAN was found to be highly resistant to electron beam irradiation and mass loss as compared to PMMA under the same beam conditions. 41,42 Therefore, PMMA-rich phases appeared brighter and SAN-rich phases darker in a typical TEM image. We noted the occurrence of ~100 nm diameter spots that remained entirely within the darker, SAN-rich domains. To the best of our knowledge, black spots in PMMA/SAN blend morphology have not been reported in previous literature on PMMA/SAN systems. 31-33,40,43 We hypothesize that these spots are due to the polydispersity of the acrylonitrile (AN) content in SAN.

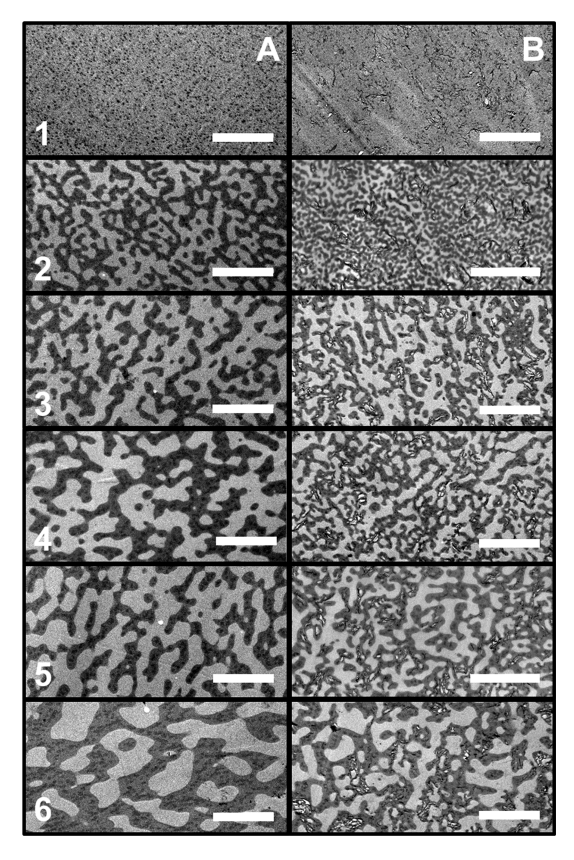


**Figure 2.** Representative cross-sectional TEM images of 70/30 PMMA/SAN neat blends (column A) or 70/30/1 PMMA/SAN/GNP ternary blends (column B) obtained under different annealing temperature and times (row 1 at 170 °C for 10 min; rows 2–6 at 200 °C for 5, 10, 20, 30, or 60 min, respectively; scale bar = 4  $\mu$ m). PMMA-rich and SAN-rich phases are the lighter and darker domains, respectively. GNPs appear as thin black lines. TEM images of 60/40 and 60/40/1 blends are included in Figure S6.

When blended with PMMA, SAN with higher wt % AN will exhibit a lower LCST than those with lower wt % AN and therefore phase separate first. Their higher wt % AN led to the dark spots. The AN-rich SAN chains likely arise from the composition drift during free-radical polymerization. The presence of the black spots does not influence our discussion on the effect of GNPs in CPCs. Hence, we will leave further discussions of these black domains in a future publication.

For ternary PMMA/SAN/GNP blends, GNPs appear as thin black lines due to their higher electron density. Before phase separation, GNPs were shown to be randomly and uniformly distributed within the polymer matrix (Figure 2, image B1). Solution blending and sonication helped to break apart large GNP agglomerates, even though local GNP clusters still exist. After phase separation, GNPs are seen to localize exclusively in the darker SAN-rich phase due to the favorable  $\pi-\pi$  interactions between the PS components in SAN and the basal planes of GNPs. The observation is consistent with the calculated wetting coefficient  $(\omega)$  of GNP between PMMA-rich and SAN-rich phases from Young's equation

$$\omega = \cos \theta = \frac{\gamma_{\text{PMMA-rich/GNP}} - \gamma_{\text{SAN-rich/GNP}}}{\gamma_{\text{PMMA-rich/SAN-rich}}}$$
(3)

From eq 3, GNPs prefer to locate at the PMMA-rich/SAN-rich interface if  $-1 < \omega < 1$ , in the PMMA-rich phase if  $\omega < -1$ ,

and in the SAN-rich phase if  $\omega > 1$ . As interfacial energies were not available from previous literature, we estimated them from the surface energies of each component using the Owens–Wendt equation 44,45

$$\gamma_{1/2} = \gamma_1 + \gamma_2 - 2\sqrt{\gamma_1^d \gamma_2^d} - 2\sqrt{\gamma_1^P \gamma_2^P}$$
(4)

Here,  $\gamma_k^{\rm d}$  and  $\gamma_k^{\rm p}$  represent the dispersive and polar components of the surface energy of component k, respectively. We further estimated the surface energies of PMMA-rich and SAN-rich phases using volume-averaged values of the pure species. The details of the calculation are provided in the Supporting Information, section S3. From the Owens–Wendt equation, we have  $\gamma_{\rm PMMA-rich/SAN-rich} = 0.058~{\rm mJ/m^2}$ ,  $\gamma_{\rm PMMA-rich/GNP} = 4.69~{\rm mJ/m^2}$ , and  $\gamma_{\rm SAN-rich/GNP} = 4.45~{\rm mJ/m^2}$ . Therefore, the wetting coefficient was  $\omega = 4.0$ , suggesting that GNPs prefer to localize in the SAN-rich phase upon phase separation.

TEM imaging provides a powerful tool to quantitatively characterize the effect of GNPs on the blend morphology after phase separation. In the following section, we will analyze the effect of GNPs on both the local and bulk morphology after phase separation and subsequent annealing.

3.3. Image Analysis. The local effect of GNPs on the blend morphology was characterized by using domain crosscorrelation analysis, which allowed us to determine the location of GNPs relative to the phase-separated morphology. Figure 3 shows the general schematic of our analysis. First, we segmented each TEM image to extract PMMA, SAN, and GNP domains into three mutually exclusive binary square matrices using the Trainable Weka Segmentation toolkit in FIJI. 46 Next, we computed the 2D cross-correlation matrix between two segmented domains of interest. For an image with dimension of  $n \times n$  pixels, the corresponding 2D crosscorrelation matrix has dimensions of  $(2n-1) \times (2n-1)$ , where the value at the  $(n + r_x, n + r_y)$  index represents the correlation value when the first segmented domain is offset by  $\vec{r} = (r_x, r_y)$  with respect to the second segmented domain. To eliminate the amplitude dependence of segmented domains, the cross-correlation was normalized to values between -1 and 1, representing the limiting cases of having a pair of anticorrelated or fully correlated images, respectively. This analysis was implemented using the MATLAB function normxcorr2 developed by Lewis<sup>47</sup> and Haralick et al.<sup>48</sup>

Figure 3c shows the pairwise cross-correlation matrices of the sample image between PMMA, SAN, and GNP domains around the origin (n, n) where the two segmented domains are overlaid with each other. The field of view was chosen to be ±510 nm. Because the segmented domains are complementary, the cross-correlation coefficients at the origin always approach -1. When the first segmented domain is offset with respect to the second one, their overlapping extracted features give rise to the cross-correlation intensity. By radially averaging the 2D cross-correlation around the origin (Figure 3d), we observe a peak at  $\sim$ 55 nm for SAN  $\times$  GNP and a peak at  $\sim$ 360 nm for PMMA × SAN. The occurrence of each peak represents a characteristic length  $\lambda_{[A \times B]}$  between A and B domains. For example,  $\lambda_{[SAN\times GNP]}$  reflects the mean distance of a GNP sheet to its nearest SAN-rich phase interface, whereas  $\lambda_{[PMMA \times SAN]}$  reflects the average lateral size of PMMA-rich phase surrounded by SAN. Because GNPs did not localize within the PMMA-rich phases, no apparent peak was observed for  $\lambda_{[PMMA\times GNP]}$  in the field of view.

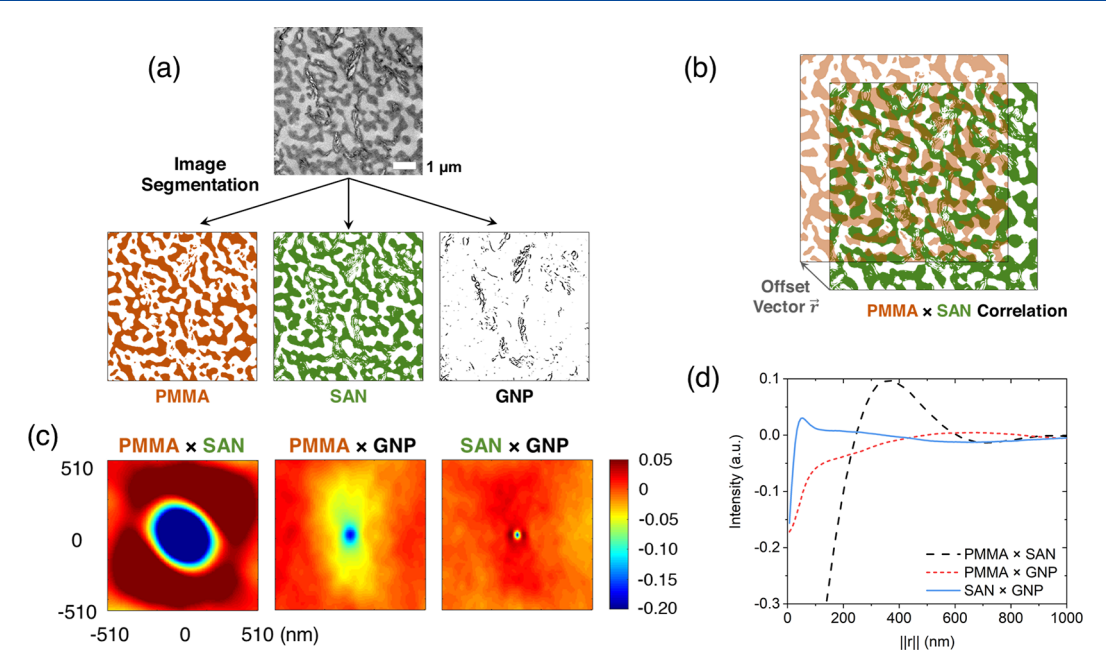


Figure 3. 2D cross-correlation between different domains in PMMA/SAN/GNP blends after phase separation: (a) image segmentation to isolate different components of a 70/30/1 PMMA/SAN/GNP blend annealed at 200 °C for 20 min; (b) cross-correlation with an offset vector  $\vec{r}$  (in this schematic  $|\vec{r}| = 0.85 \ \mu \text{m}$ ); (c) pairwise cross-correlation coefficients between PMMA, SAN, and GNP domains; (d) radially averaged cross-correlation intensity obtained from (c).

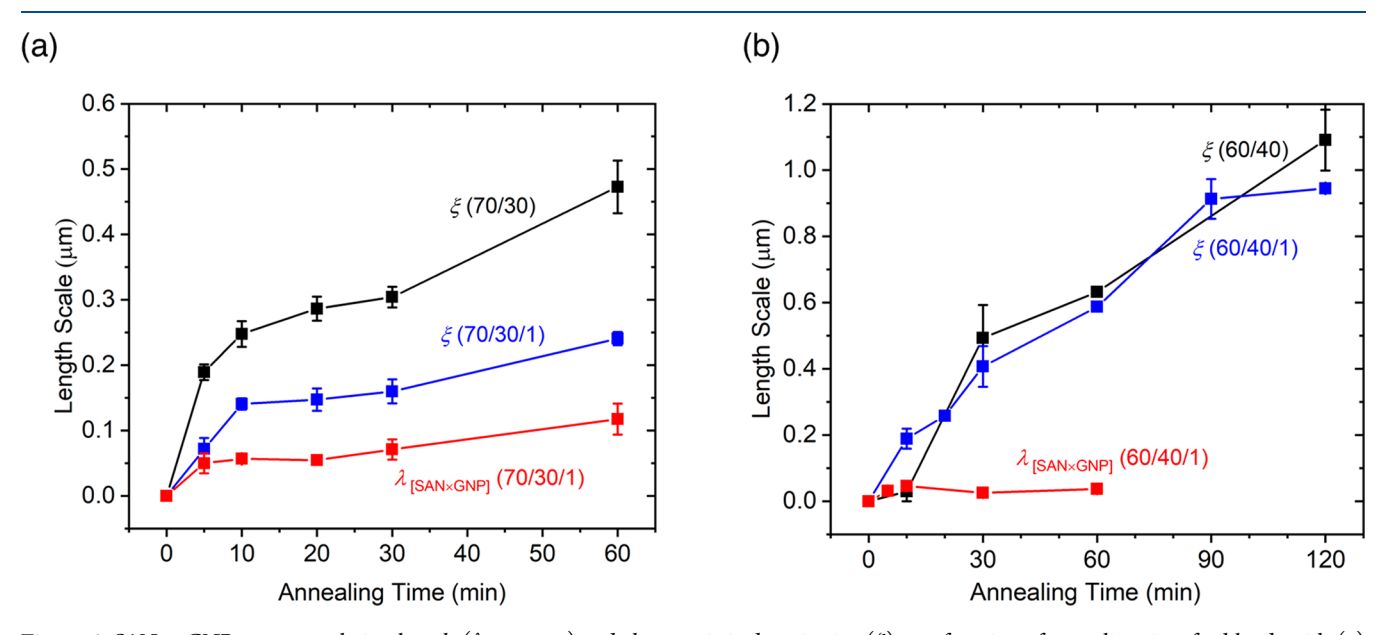
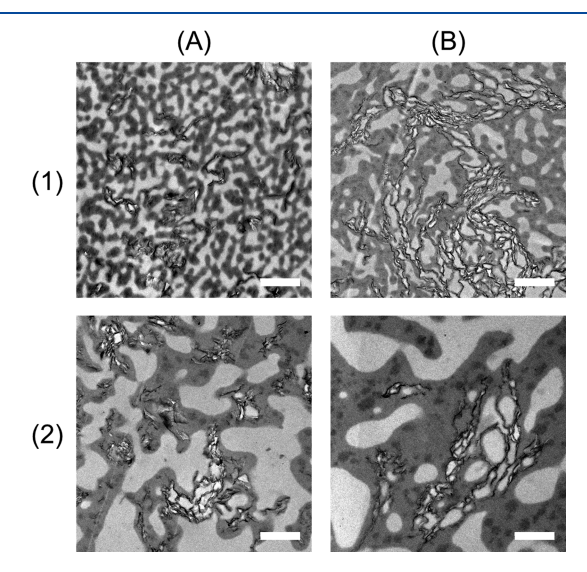


Figure 4. SAN × GNP cross-correlation length ( $\lambda_{[SAN\times GNP]}$ ) and characteristic domain size ( $\xi$ ) as a function of annealing time for blends with (a) 70/30 and (b) 60/40 PMMA/SAN composition.

The cross-correlation of SAN × GNP in the PMMA/SAN/GNP blends quantifies the length scale over which SAN nucleates around GNP surfaces during phase separation. A series of TEM images of the same magnification representing PMMA/SAN/GNP blends annealed at 200 °C for different times were used in this analysis. The corresponding characteristic cross-correlation length,  $\lambda_{\rm [SAN\times GNP]}$ , is shown in Figure 4. For PMMA/SAN/GNP ternary blends during the initial stages of annealing,  $\lambda_{\rm [SAN\times GNP]}$  showed a plateau value of 25–50 nm within the first 30 min for both 70/30/1 and 60/40/1 blends, which corresponds to a thickness of (2–4) $R_{\rm g}$  of SAN polymers (corresponding to their measured  $M_{\rm w}$ ) along GNP surfaces. This characteristic thickness represents the length scale over

which the interaction between polymers and filler particles becomes important during phase separation, resulting in the thermodynamically preferred nucleation of SAN along the GNP surfaces. The observation of surface layer formation around fillers upon phase separation was reported in several earlier works. <sup>39,40</sup> For longer annealing times up to 60 min,  $\lambda_{\rm [SAN\times GNP]}$  continued to grow to ~100 nm for the 70/30/1 samples due to domain coalescence. On the other hand,  $\lambda_{\rm [SAN\times GNP]}$  remained constant at ~25 nm for the 60/40/1 samples. We believe the growth of the SAN surface layer thickness may be affected by the dispersion and exfoliation of GNP sheets in the blend. In general, GNP sheets were seen to be better dispersed in the 70/30/1 than the 60/40/1 blends

(as shown by comparing Figure 5, columns A and B). This may be due to the higher matrix viscosity of the 60/40/1 blends



**Figure 5.** TEM images of 70/30/1 (column A) or 60/40/1 (column B) blends annealed at 200 °C for 5 min (row 1) or 60 min (row 2). Scale bar = 1  $\mu$ m.

since it contains a higher composition of the more viscous SAN component. GNP sheets that were exfoliated and better dispersed appeared more stretched in the blend. This allowed the surrounding SAN surface layer to coalesce with SAN chains in the bulk, causing the surface layer thickness to grow. On the other hand, the more aggregated GNP fillers act as physical confinements to impede the SAN surface layer from interacting with any surrounding SAN chains in the bulk, thereby limiting the surface layer growth.

With the formation of SAN surface layers around GNP sheets upon phase separation, the surrounding PMMA chains were expelled toward the interstitial spaces confined by GNP

fillers. As seen in Figure 5, this led to the formation of a number of PMMA-rich domains with lateral sizes smaller than the PMMA-rich domains far away from GNPs, resulting in blend morphologies different from PMMA/SAN spinodal decomposition alone. In addition, the lateral dimensions of these domains were stable during longer annealing periods of up to 60 min, since these domains were bounded by both GNP sheets and the surrounding SAN surface layers. The effect of GNP on domain coarsening will be addressed in the upcoming section.

The effect of GNPs on the bulk morphology was analyzed by calculating the area fraction corresponding to each of component obtained from image segmentation. Results are shown in Figure 6. For the 70/30 neat blends, the area fractions of PMMA-rich and SAN-rich phases were ~55/45%. This result agrees with the lever rule calculation using the phase diagram, which predicts that the PMMA-rich phase to be ~59 vol % (see the Supporting Information, section S5, for calculation details). Furthermore, the area fraction each segmented domain remained constant within error bars over the entire duration of annealing, suggesting that the diffusion of polymer species between PMMA-rich and SAN-rich domains was negligible once phase separation had occurred. As for the 70/30/1 blends, the area fraction of the PMMArich, SAN-rich, and GNP-rich phases were ~40/56/4%. Note that the area fraction of GNP-rich phases was considerably higher than the volume fraction of pure GNP, ~0.5% (assuming  $\rho_{\rm GNP} \sim 2.2 \ {\rm g/cm^3}$ ). This was due to the fact that TEM images were of lower magnification; analysis was limited by pixel resolution, ~15 nm/pixel. Consequently, the majority of the segmented GNP-rich phases represent SAN surface layers that formed around GNPs. Thus, compared to the 70/ 30 blends, the area fraction of SAN-rich phase of the ternary blends increased from ~45% to ~60%. This result indicates that the SAN-rich phase now contains a higher PMMA concentration than in the binary blends. It is not clear what caused the area fraction of the SAN-rich phase to increase in

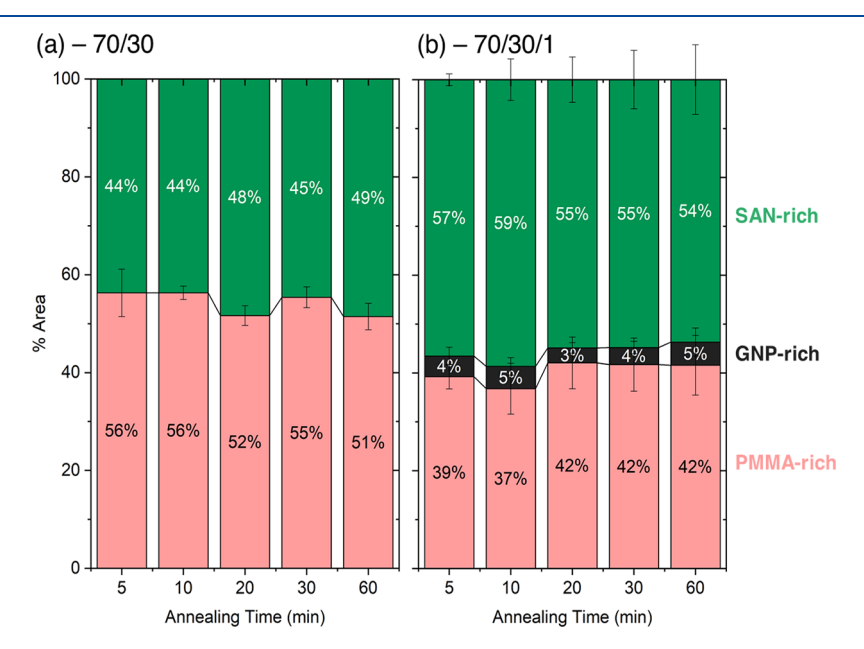


**Figure 6.** Area fractions corresponding to PMMA-rich, SAN-rich, and GNP-rich domains calculated from segmented TEM images for (a) 70/30 blends and (b) 70/30/1 blends for different annealing times at 200 °C. Error bars represent the standard deviation from averaging at least three TEM images of each sample.

the ternary blends. One possible explanation may be due to the selective adsorption of low molecular weight PMMA chains at GNP surfaces during solvent mixing prior to phase separation. <sup>39,49,50</sup> We posit that the polymer composition of the SAN-rich phase near GNP surface would be higher in the low molecular weight component PMMA. The composition of polymer blend at a free surface can be affected by the molecular weight disparity of the two blend species.<sup>49</sup> As confining a polymer chain near a free surface decreases its conformational entropy, shorter polymer chains require lower entropic penalty and would have preferential partitioning to the surface if entropic effects dominate over enthalpic ones. In our system, while SAN has more favorable enthalpic interaction with the GNP than PMMA,  $M_{\rm n,SAN}$  (= 73 kg/ mol) is also higher than  $M_{\rm n,PMMA}$  (= 20 kg/mol). We believe the molecular weight disparity between SAN and PMMA is significant enough for the entropic effects to dominate, in order that the low molecular weight species partition to the surface. In the ternary blends, smaller PMMA-rich domains sandwiched in-between GNP sheets also appeared brighter than PMMA-rich domains in the bulk (Figure 5). This may indicate either these smaller bright domains contain a higher PMMA concentration or GNPs promote degradation of PMMA under the electron beam irradiation during TEM imaging.51

**3.4. Domain Coarsening.** Coarsening between PMMArich and SAN-rich domains during annealing is expected to be similar to that of immiscible blends, as the diffusion of polymer species between PMMA-rich and SAN-rich domains was not present in our previous analysis. However, the presence of GNPs can influence the rate of domain coarsening during annealing. To quantify the evolution of polymer domain sizes during annealing, we calculated the characteristic domain size  $(\xi)$  to study domain coarsening as a function of annealing times.  $\xi$  represents the average thickness of co-continuous polymer domains and is defined by

$$\xi \equiv \frac{A}{L_{\rm int}} \tag{5}$$

where  $L_{\rm int}$  is the total interfacial length and A the total area of a TEM image. This metric has been used in our previous work on co-continuous polymer blends,  $^{52}$  polymer blend composites,  $^{21,53}$  and bijels.  $^{26}$  The definition of  $\xi$  relates to the inverse of the total interfacial area per unit volume, which is often referenced by earlier literature.  $^{54,55}$  We processed the TEM images by first extracting the PMMA/SAN-rich phases via image segmentation and then calculating the interfacial length by using a MATLAB code. At least five images with dimensions of at least 10  $\mu{\rm m}\times$  10  $\mu{\rm m}$  for each sample were used in the calculation.

Figure 4 shows the evolution of  $\xi$  as a function of annealing time at 200 °C. The initial rate of domain coarsening,  $\mathrm{d}\xi/\mathrm{d}t$ , representing the coalescence of interfacial area, was found to be  $\sim\!0.025~\mu\mathrm{m/min}$  for the 70/30 blend and  $\sim\!0.017~\mu\mathrm{m/min}$  for the 60/40 blend. Theoretically, the rate of domain coarsening can be expressed as 53,56

$$\frac{\mathrm{d}\xi}{\mathrm{d}t} = \beta \frac{\gamma}{\eta_{\mathrm{blend}}} \tag{6}$$

where  $\gamma = 0.27 \text{ mJ/m}^2$  (PMMA/SAN interfacial energy) and  $\eta_{\text{blend}} = 2 \times 10^4 \text{ Pa·s}$  (zero shear viscosity measured by rheology, Figure S3) at 200 °C. The dimensionless factor  $\beta$ 

was calculated to be 0.031 for the 70/30 blend and 0.021 for the 60/40 blend. These values are in agreement with the average value of  $\beta \sim 0.03$  found by Hedegaard et al. in reviewing literature data on the coarsening of 30 different cocontinuous blends. While the 60/40 blend exhibited a uniform linear coarsening rate during annealing, the 70/30 blend showed an apparent two-stage coarsening dynamics, in which coarsening initially followed a fast linear growth rate but slowed down after 10-20 min of annealing. This two-stage coarsening behavior has been previously observed in cocontinuous PS/PE<sup>57</sup> and fluorescently labeled PS/SAN<sup>58</sup> blends by using multiple 3D imaging techniques.

Figure 4 compares the evolution of  $\xi$  of both 60/40/1 and 70/30/1 ternary blends to the corresponding neat blends. For the 70/30/1 blends,  $\xi$  is consistently lower than that of the 70/ 30 neat blends by a factor of  $\sim$ 2. In this case, GNPs effectively suppress coarsening of the bulk polymer matrix. The slowdown of coarsening arose mainly from the viscosity increase of the SAN-rich phase due to GNP localization. Additionally, the morphology of the 70/30 blend was more co-continuous and spatially regular than the 70/30/1 blends. In particular, we observed a number of polymer domains that were much smaller in lateral dimension near surfaces of GNP fillers compared to regions without GNP presence. Because GNPs act as nucleation sites for SAN chains in proximity to the filler surface during the early stage of spinodal decomposition, the unfavorable PMMA chains were expelled outward from the thin layer of SAN surrounding GNP surfaces to form domains with smaller lateral dimensions. The smaller PMMA-rich domains formed around GNPs also appeared brighter than the PMMA-rich domains in the bulk under TEM. This may suggest that the smaller PMMA-rich domains have higher PMMA concentration and therefore more prone to degradation under the electron beam.<sup>41</sup> Coupled with the low thermal diffusivity of GNP in the polymer blend, these fine polymer domains in proximity to GNP surfaces were preserved during longer annealing times (Figure 5). To further illustrate this, we compared the distribution of 70/30 and 70/30/1 blends' interfacial perimeters as a function of annealing time using several TEM images (Figure S7). Spinodal decomposition created log-normal interfacial perimeter distribution for the 70/30 blends whose mean value increases with annealing time. As for the 70/30/1 blends, we observed a much higher number of smaller polymer domains forming near GNP fillers. The smaller polymer phases were seen to be stable with respect to longer annealing time, which suppressed the growth of the log mean interfacial perimeter length with time and resulted in a skewed interfacial perimeter distribution. On the other hand, both 60/40 and 60/40/1 blends show similar rate of domain coarsening during annealing. As evidenced by TEM images (Figure S6), both 60/40 and 60/40/1 blends phase separate into droplet-matrix morphologies. As many GNP aggregates of the 60/40/1 blend became well encapsulated within the SANrich phase, many large PMMA-rich droplets >1  $\mu$ m in lateral dimension were formed far away from GNP aggregates. These PMMA-rich droplets coarsened during annealing similar to binary blends. Therefore, GNP fillers with better dispersion can act more strongly to suppress domain coarsening and preserve the initial morphology.

In summary, GNPs induced local nucleation of the more favorable SAN chains upon phase separation into surface layers of  $\sim 4R_{\rm g}$  in thickness and enlarged the area fraction of SAN-rich domains in the bulk. GNPs also suppressed domain

Table 2. Bulk DC Conductivity (S/cm) at 25 °C of PMMA/SAN and PMMA/SAN/GNP Blends Prepared at Different Annealing Temperatures and Times<sup>a</sup>

blend composition	170 °C, 10 min	200 °C, 10 min	200 °C, 20 min	200 °C, 30 min	200 °C, 60 min
neat blends	<10 <sup>-15</sup>				
70/30/1	<10 <sup>-15</sup>	$1.7 \times 10^{-14}$	$2.3 \times 10^{-14}$	$4.3 \times 10^{-10}$	$6.4 \times 10^{-10}$
60/40/1	$2.3 \times 10^{-14}$	$7.5 \times 10^{-9}$	$6.8 \times 10^{-8}$	$8.2 \times 10^{-8}$	$5.2 \times 10^{-8}$

<sup>a</sup>Typical measurement errors are  $\pm 15\%$ .

coarsening of the co-continuous blend by increasing the SAN-rich domain viscosity and promoting the formation of smaller PMMA domains in-between SAN surface layers, which were stable during longer annealing times. Overall, the presence of GNPs led to the formation of unique ternary blend morphology that is different from the morphology resulted from spinodal decomposition alone.

**3.5. Electrical Conductivity.** Finally, the bulk electrical conductivity ( $\sigma$ ) of the PMMA/SAN/GNP blends was measured in the out-of-plane direction using the two-point probe technique to evaluate their performance as potential CPCs (Table 2). We believe the bulk electrical conductivity of our composites was isotropic, since TEM images reveal their morphologies to be isotropic: GNPs were initially randomly dispersed in the blend and co-continuous domains formed by PMMA/SAN spinodal decomposition were spatially random. Ternary blends prior to phase separation were nonconductive; upon phase separation,  $\sigma$  increased by 5-7 orders of magnitude and remained approximately constant during annealing at 200 °C for 60 min. The enhancement in electrical conductivity was due to the selective localization of GNPs in the SAN-rich phases upon spinodal decomposition. GNP sheets percolate within the co-continuous SAN-rich phases, which have a higher effective filler concentration.

To continuously monitor possible microstructural changes, we performed simultaneous measurement of shear rheology and complex conductivity at 200 °C. For comparison, we also performed the same measurements using two control SAN/GNP samples prepared using similar probe sonication and solvent mixing procedures. These blends are denoted as SAN/x, where x denotes the wt % of GNP. The real part of the complex electrical conductivity ( $\sigma'$ ) was measured at  $\omega_{\rm ac}$  = 20 Hz, which approaches the dc conductivity (Figure S9). These results are shown in Figure 7.

Initially,  $\sigma'$  values of the 70/30/1 and 60/40/1 blends were over 4 orders of magnitude apart:  $\sigma'$  of the 70/30/1 blend was similar to that of SAN/1 while  $\sigma'$  of the 60/40/1 blend was similar to that of SAN/2. Upon further annealing,  $\sigma'$  of the 70/ 30/1 blend improves by 4 orders of magnitude while  $\sigma'$  of the 60/40/1 blend remains within the same order of magnitude. To understand the seemingly different effect of annealing on the sample conductivity, samples' time-resolved rheological characteristics were analyzed in conjunction with their electrical conductivity. In Figure 7, the evolution of  $\sigma'$  and storage modulus G' of each sample was plotted simultaneously during annealing. For the control samples, G' consists of contributions from both the polymer matrix  $(G'_{mat})$  and GNP  $(G'_{GNP})$ . In Figure 7a,b, both SAN/1 and SAN/2 blends saw gradual increases in G' during annealing. As both control samples only contain SAN as the polymer matrix,  $G'_{mat}$  must remain constant during annealing. Thus, the observed increase in G' must be due to  $G'_{GNP}$ , indicating GNPs had undergone rearrangement and structure recovery during quiescent annealing.<sup>15</sup> This led to a better percolated filler network

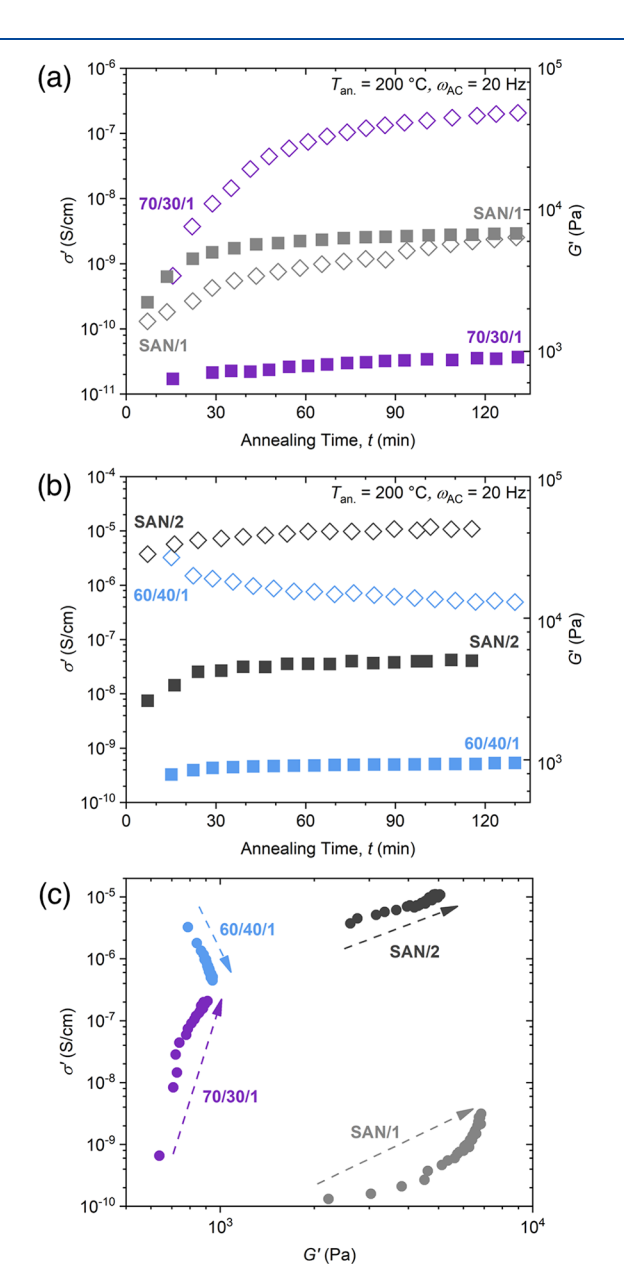


Figure 7. (a, b) Evolution of  $\sigma'(\diamondsuit)$  and  $G'(\blacksquare)$  as a function of annealing time during isothermal time sweep experiments at 200 °C, shear frequency 0.1 rad/s, and ac frequency of 20 Hz for (a) 70/30/1 and SAN/1 blends and (b) 60/40/1 and SAN/2 blends. The data are replotted in (c) to show the correlation of  $\sigma'$  vs G'; the arrows point in the direction of increasing annealing time over 2 h.

within the polymer matrix, leading to an increase in  $\sigma'$ . These results agree with room temperature dc conductivity measurements reported in Table 3. Our claim is further corroborated with an estimation of filler diffusion in the melt. Assuming the hydrodynamic radius of an average GNP sheet is  $R_{\rm h} \sim 450$ 

Table 3. Bulk DC Conductivity (S/cm) at 25 °C of SAN/1 and SAN/2 Blends before and after Annealing

blend composition	unannealed	200 °C, 150 min
SAN/1	$2.0 \times 10^{-14}$	$7.5 \times 10^{-14}$
SAN/2	$1.5 \times 10^{-9}$	$2.3 \times 10^{-8}$

nm,<sup>59</sup> the time required for a GNP sheet to diffuse over a typical length of  $d \sim 20$  nm (measured from TEM images) to an adjacent GNP sheet, is estimated to be  $t=\frac{\pi\eta R_{\rm h}\langle d^2\rangle}{kT}\sim 30$ min, which falls within the range of annealing times in this study. On the other hand, G' of phase-separated PMMA/ SAN/GNP ternary composites receives a contribution from  $G'_{\rm mat}$ ,  $G'_{\rm GNP}$ , and the interfacial elasticity between polymer domains  $(G'_{\rm int})^{26,60}$  While domain coarsening between neat polymer blends reduces the total interfacial area between polymer domains and leads to a decrease in  $G'_{\text{int}}$   $^{26,30,61}$  G' of both 70/30/1 and 60/40/1 blends continued to increase during the annealing as shown in Figure 7a,b. This suggests that  $G'_{GNP}$  contributes more than  $G'_{int}$  to the overall G' of the ternary blends, an observation consistent with the lowfrequency slopes of G' observed in PMMA/SAN/GNP blends, SAN/GNP blends, and PMMA/SAN neat blends (Figure S10). The continuous increase of G' in the ternary blends during annealing further indicates the similar conformation rearrangement of GNP sheets into a better percolated filler network. It is notable that the G' of the SAN/GNP blends were higher than those of either ternary blend samples after annealing because the SAN polymer has a much higher molecular weight than PMMA and that the SAN/GNP blends have higher SAN content than the ternary blends. It was found that the G' values of SAN and PMMA neat polymers at 200 °C in the terminal flow regime ( $\omega \leq 1 \text{ rad/s}$ ) were more than 2 orders of magnitude apart (Figure S3).

In Figure 7c,  $\sigma'$  is plotted versus G' to further clarify the correlation between the electrical conductivity and blend morphology. For both SAN/1 and SAN/2 blends,  $\sigma'$  positively correlates with G' during annealing since the connectivity of GNPs was improved. The 70/30/1 blends also see this positive correlation because the SAN-rich domains are believed to maintain bulk continuity during annealing, which preserves the conductive pathways of GNPs contained therein. For the 60/ 40/1 blend,  $\sigma'$  negatively correlates with G' during annealing because the PMMA-rich domains eventually coarsen into droplets that are comparable to local GNP clusters. Even though the GNP sheet connectivity within each localized aggregate improves with the increase in G', the larger PMMArich droplets breaks off continuous paths of the SAN-rich domains and isolates GNP clusters from forming a conductive network in the bulk (Figure S6).

The time evolution of  $\sigma'$  during annealing at 200 °C was in agreement with Table 2 in that the composite conductivity increased upon PMMA/SAN phase separation and that after sufficient annealing both 70/30/1 and 60/40/1 conductivities were comparable to that of SAN/2 within the same order of magnitude. We acknowledge our composites appear more electrically conductive in the melt: the sample  $\sigma'$  measured at 200 °C by using the rheodielectric apparatus was  $\sim$ 2 orders of magnitude higher than the room temperature conductivity values reported in Table 2. As the rheodielectric measurement was made above the glass transition temperature, polymer chains are thermally expanded from glassy state to an

amorphous state. This reduces the interparticle gap width and increases contact points between adjacent fillers, leading to an increased electrical conductivity.<sup>62</sup> We provide in the Supporting Information, section S6.2, more discussion on this.

The low-frequency, low-amplitude ( $\leq 0.1 \text{ rad/s}, \leq 10\%$ ) shearing during our rheodielectric measurements can be regarded as quasi-quiescent and does impart change to the composites' electrical conductivity different from quiescent annealing. Oscillatory shear of low to moderate shear amplitudes deforms the filler network reversibly. Previous literature has reported the time-resolved dependence of the electrical conductivity of a polycarbonate/multiwall carbon nanotube (PC/MWCNT) blends under sinusoidal shear with a moderate 50% strain amplitude and 1 rad/s frequency. It was found that the PC/MWCNT blend conductivity stayed within  $\pm 5\%$  of the mean value during the steady-state oscillatory shear. In addition, the electrical conductivity oscillates with the square of the applied strain rate, reaching the maximum value at zero strain and the minimum value at the reversal point of the strain oscillation. 63 The reversible network deformation of the filler network under oscillatory shear has been described as a "memory effect". Upon the applied strain, the conductive filler network is partially deformed and conductivity decreases. But upon reaching the reversal point of the strain oscillations, the filler network returns to the previous position to re-form the original filler network, and thus the conductivity is restored. Because both the strain amplitude and frequency used in our experiments were both much lower, the effect of oscillatory shear on the overall electrical conductivity of the composites is negligible over the time resolution of each measurement data point ( $\sim 60$  s). Thus, the quiescent annealing and low-amplitude oscillatory shearing will have similar effect on the electrical conductivity of our composites if performed at the same temperature.

Based on the discussions above, enhancing the electrical conductivity of the PMMA/SAN/GNP blend upon phase separation requires both long-range connectivity of GNP fillers and the continuity of SAN-rich domains. For similar systems, it is desirable to determine a suitable annealing time that promotes the formation of interconnected GNP network while preserving the polymer domain connectivity to achieve the highest electrical conductivity.

## 4. CONCLUSION

In summary, our work demonstrates the possibility to create CPCs using miscible polymer blends of commercial PMMA/SAN with conductive GNP fillers. The phase diagram of PMMA/SAN blends near the critical composition was constructed by using a combination of cloud point measurements and rheology, allowing us to prepare PMMA/SAN-rich phase-mixed samples below the LCST and induce spinodal decomposition at 200 °C to obtain co-continuous polymer morphology.

TEM images show that PMMA and SAN were initially in a miscible state but phase separate into distinct domains when heated above LCST. GNPs preferentially localized in the SAN-rich phase upon spinodal decomposition, which is consistent with wetting coefficient calculations. By performing image segmentation and cross-correlation analysis, we further extracted a length scale that corresponds to  $(2-4)R_{\rm g}$  of the SAN chains surrounding GNPs, which suggests the nucleation of SAN on the GNP surfaces during phase separation. As a result, the presence of GNPs results in unique blend

morphology consisting of thin layers of SAN-rich phases near their surface and encapsulated PMMA-rich phases within SAN. The polymer domain sizes near GNPs were much smaller compared to the bulk and were found to be stable during annealing. By calculating the evolution of the characteristic domain size from TEM images, we also found that blends with co-continuous morphology and better dispersed GNP fillers will more strongly suppress coarsening during annealing.

Finally, we saw that the electrical conductivity of PMMA/SAN/GNP blends was significantly enhanced upon phase separation. The selective localization of GNPs within the SAN-rich phases enhances their effective concentration within the polymer blend, while annealing for longer times can further improve the connectivity of GNP sheets. Maintaining longrange connectivity of SAN-rich phases and contact between GNP fillers were both found to be crucial to enhance the blend's electrical conductivity.

This work introduces a facile method to construct CPCs by inducing spinodal decomposition in miscible polymer blends. By use of a two-step solvent blending/annealing process, the resulting composite shows co-continuous and spatially regular morphology in which conductive GNP fillers percolate entirely within the SAN-rich phase. Based on room temperature conductivity measurements, samples at 1 wt % GNP loading achieved electrical conductivity levels that fall in range of ESD protection packaging materials. The electrical conductivity of the samples may be further enhanced by improving the dispersion of GNPs in the polymer matrix. Further reduction in the percolation threshold may be achieved if the fillers localize at the continuous interfaces between polymers. 21,23,26 Future work will focus on controlling the wettability of GNPs by grafting polymer chains on their surfaces to promote their interfacial localization between polymer blends.

## ASSOCIATED CONTENT

## **S** Supporting Information

The Supporting Information is available free of charge on the ACS Publications website at DOI: 10.1021/acs.macromol.9b01391.

Characterization of neat polymers, measurement of the PMMA/SAN phase diagram, surface energy calculation, additional TEM images, image analysis of relative phase content and PMMA/SAN domain size distribution, and further discussion on electrical conductivity (PDF)

## AUTHOR INFORMATION

## **Corresponding Authors**

\*E-mail xcheng@umn.edu (X.C.).

\*E-mail macosko@umn.edu (C.W.M.).

ORCID ®

Yangming Kou: 0000-0002-9863-548X Xiang Cheng: 0000-0002-2759-764X

Christopher W. Macosko: 0000-0002-2892-3267

Notes

The authors declare no competing financial interest.

## ACKNOWLEDGMENTS

We gratefully acknowledge funding from the National Science Foundation (CMMI-1661666). Parts of this work were performed in the Characterization Facility, University of Minnesota, a member of the NSF-funded Materials Research Facilities Network (www.mrfn.org) via the MRSEC program.

#### REFERENCES

- (1) Technavio. Global Conductive Polymers Market 2017–2021, 2017.
- (2) Pang, H.; Xu, L.; Yan, D. X.; Li, Z. M. Conductive Polymer Composites with Segregated Structures. *Prog. Polym. Sci.* **2014**, 39 (11), 1908–1933.
- (3) Geetha, S.; Satheesh Kumar, K. K.; Rao, C. R. K.; Vijayan, M.; Trivedi, D. C. EMI Shielding: Methods and Materials-A Review. *J. Appl. Polym. Sci.* **2009**, *112* (4), 2073–2086.
- (4) Chung, D. D.; D, L. Electromagnetic Interference Shielding Effectiveness of Carbon Materials. *Carbon* **2001**, 39 (2), 279–285.
- (5) Li, N.; Huang, Y.; Du, F.; He, X.; Lin, X.; Gao, H.; Ma, Y.; Li, F.; Chen, Y.; Eklund, P. C. Electromagnetic Interference (EMI) Shielding of Single-Walled Carbon Nanotube Epoxy Composites. *Nano Lett.* **2006**, *6* (6), 1141–1145.
- (6) Electrostatic Discharge Association. ANSI/ESD S541-2018: Packaging Materials for the Protection of Electrostatic Discharge Susceptible Item, 2018.
- (7) Lee, B.-L. Permanently Electrostatic Dissipative (ESD) Property via Polymer Blending: Rheology and ESD Property of Blends of PETG/ESD Polymer. *J. Appl. Polym. Sci.* 1993, 47 (4), 587–594.
- (8) Balberg, I. A Comprehensive Picture of the Electrical Phenomena in Carbon Black-Polymer Composites. *Carbon* **2002**, *40* (2), 139–143.
- (9) Nan, C.-W.; Shen, Y.; Ma, J. Physical Properties of Composites Near Percolation. *Annu. Rev. Mater. Res.* **2010**, *40* (1), 131–151.
- (10) Miyasaka, K.; Watanabe, K.; Jojima, E.; Aida, H.; Sumita, M.; Ishikawa, K. Electrical Conductivity of Carbon-Polymer Composites as a Function of Carbon Content. *J. Mater. Sci.* **1982**, *17* (6), 1610–1616.
- (11) Sumita, M.; Abe, H.; Kayaki, H.; Miyasaka, K. Effect of Melt Viscosity and Surface Tension of Polymers on the Percolation Threshold of Conductive-Particle-Filled Polymeric Composites. *J. Macromol. Sci., Part B: Phys.* **1986**, 25 (1–2), 171–184.
- (12) Sumita, M.; Sakata, K.; Asai, S.; Miyasaka, K.; Nakagawa, H. Dispersion of Fillers and the Electrical Conductivity of Polymer Blends Filled with Carbon Black. *Polym. Bull.* **1991**, *25* (2), 265–271.
- (13) Wang, Y.; Weng, G. J. Electrical Conductivity of Carbon Nanotubeand Graphene-Based Nanocomposites. In *Micromechanics and Nanomechanics of Composite Solids*; Meguid, S. A., Weng, G. J., Eds.; Springer International Publishing: 2018; pp 123–156.
- (14) Stankovich, S.; Dikin, D. A.; Dommett, G. H. B. B.; Kohlhaas, K. M.; Zimney, E. J.; Stach, E. A.; Piner, R. D.; Nguyen, S. B. T.; Ruoff, R. S. Graphene-Based Composite Materials. *Nature* **2006**, 442 (7100), 282–286.
- (15) Kim, H.; Macosko, C. W. Morphology and Properties of Polyester/Exfoliated Graphite Nanocomposites. *Macromolecules* **2008**, 41 (9), 3317–3327.
- (16) Gubbels, F.; Jérôme, R.; Teyssié, P.; Vanlathem, E.; Deltour, R.; Calderone, A.; Parenté, V.; Brédas, J. L. Selective Localization of Carbon Black in Immiscible Polymer Blends: A Useful Tool To Design Electrical Conductive Composites. *Macromolecules* **1994**, 27 (7), 1972–1974.
- (17) Gubbels, F.; Blacher, S.; Vanlathem, E.; Jérôme, R.; Deltour, R.; Brouers, F.; Teyssié, P. Design of Electrical Conductive Composites: Key Role of the Morphology on the Electrical Properties of Carbon Black Filled Polymer Blends. *Macromolecules* **1995**, 28 (5), 1559–1566.
- (18) Wu, D.; Zhang, Y.; Zhang, M.; Yu, W. Selective Localization of Multiwalled Carbon Nanotubes in Poly( $\varepsilon$ -Caprolactone)/Polylactide Blend. *Biomacromolecules* **2009**, *10* (2), 417–424.
- (19) Göldel, A.; Marmur, A.; Kasaliwal, G. R.; Pötschke, P.; Heinrich, G. Shape-Dependent Localization of Carbon Nanotubes and Carbon Black in an Immiscible Polymer Blend during Melt Mixing. *Macromolecules* **2011**, *44* (15), 6094–6102.

(20) Qi, X.-Y. Y.; Yan, D.; Jiang, Z.; Cao, Y.-K. K.; Yu, Z.-Z. Z.; Yavari, F.; Koratkar, N. Enhanced Electrical Conductivity in Polystyrene Nanocomposites at Ultra-Low Graphene Content. ACS Appl. Mater. Interfaces 2011, 3 (8), 3130–3133.

- (21) Huang, S.; Bai, L.; Trifkovic, M.; Cheng, X.; Macosko, C. W. Controlling the Morphology of Immiscible Cocontinuous Polymer Blends via Silica Nanoparticles Jammed at the Interface. *Macromolecules* **2016**, *49* (10), 3911–3918.
- (22) Bai, L.; He, S.; Fruehwirth, J. W.; Stein, A.; Macosko, C. W.; Cheng, X. Localizing Graphene at the Interface of Cocontinuous Polymer Blends: Morphology, Rheology, and Conductivity of Cocontinuous Conductive Polymer Composites. *J. Rheol.* **2017**, *61* (4), 575–587.
- (23) Bai, L.; Sharma, R.; Cheng, X.; Macosko, C. W. Kinetic Control of Graphene Localization in Co-Continuous Polymer Blends via Melt Compounding. *Langmuir* **2018**, 34 (3), 1073–1083.
- (24) Mun, S. C.; Kim, M. J.; Cobos, M.; Gu, L.; Macosko, C. W. Strategies for Interfacial Localization of Graphene/Polyethylene-based Cocontinuous Blends for Electrical Percolation. *AIChE J.* **2019**, 65 (6), e16579.
- (25) Herzig, E. M.; White, K. A.; Schofield, A. B.; Poon, W. C. K.; Clegg, P. S. Bicontinuous Emulsions Stabilized Solely by Colloidal Particles. *Nat. Mater.* **2007**, *6* (12), 966–971.
- (26) Bai, L.; Fruehwirth, J. W.; Cheng, X.; Macosko, C. W. Dynamics and Rheology of Nonpolar Bijels. *Soft Matter* **2015**, *11* (26), 5282–5293.
- (27) Huang, C.; Gao, J.; Yu, W.; Zhou, C. Phase Separation of Poly(Methyl Methacrylate)/Poly(Styrene-Co-Acrylonitrile) Blends with Controlled Distribution of Silica Nanoparticles. *Macromolecules* **2012**, *45*, 8420.
- (28) Li, L.; Miesch, C.; Sudeep, P. K.; Balazs, A. C.; Emrick, T.; Russell, T. P.; Hayward, R. C. Kinetically Trapped Co-Continuous Polymer Morphologies through Intraphase Gelation of Nanoparticles. *Nano Lett.* **2011**, *11* (5), 1997–2003.
- (29) Bose, S.; Özdilek, C.; Leys, J.; Seo, J. W.; Wübbenhorst, M.; Vermant, J.; Moldenaers, P. Phase Separation as a Tool to Control Dispersion of Multiwall Carbon Nanotubes in Polymeric Blends. ACS Appl. Mater. Interfaces 2010, 2 (3), 800–807.
- (30) Vleminckx, G.; Bose, S.; Leys, J.; Vermant, J.; Wubbenhorst, M.; Abdala, A. A.; Macosko, C.; Moldenaers, P. Effect of Thermally Reduced Graphene Sheets on the Phase Behavior, Morphology, and Electrical Conductivity in Poly (Alpha-Methyl Styrene)-Co-(Acrylonitrile)/Poly(Methyl-Methacrylate) Blends. ACS Appl. Mater. Interfaces 2011, 3 (8), 3172–3180.
- (31) Kressler, J.; Kammer, H. W.; Klostermann, K. Phase Behavior of Poly(Methylmethacrylate) and Poly(Styrene-Co-Acrylonitrile) Blends. *Polym. Bull.* **1986**, *15* (2), 113–119.
- (32) Suess, M.; Kressler, J.; Kammer, H. W. The Miscibility Window of Poly(Methylmethacrylate)/Poly(Styrene-Co-Acrylonitrile) Blends. *Polymer* **1987**, 28 (6), 957–960.
- (33) Gao, J.; Huang, C.; Wang, N.; Yu, W.; Zhou, C. Phase Separation of Poly(Methyl Methacrylate)/Poly(Styrene-Co-Acrylonitrile) Blends in the Presence of Silica Nanoparticles. *Polymer* **2012**, *53* (8), 1772–1782.
- (34) Ni, Z. H.; Wang, H. M.; Kasim, J.; Fan, H. M.; Yu, T.; Wu, Y. H.; Feng, Y. P.; Shen, Z. X. Graphene Thickness Determination Using Reflection and Contrast Spectroscopy. *Nano Lett.* **2007**, *7* (9), 2758–2763.
- (35) Grassie, N.; Hay, J. N. Thermal Coloration and Insolubilization in Polyacrylonitrile. *J. Polym. Sci.* **1962**, *56* (163), 189–202.
- (36) Takata, T.; Hiroi, I.; Taniyama, M. Coloration in Acrylonitrile Polymers. J. Polym. Sci., Part A: Gen. Pap. 1964, 2 (4), 1567–1585.
- (37) Niu, Y. H.; Wang, Z. G. Rheologically Determined Phase Diagram and Dynamically Investigated Phase Separation Kinetics of Polyolefin Blends. *Macromolecules* **2006**, *39* (12), 4175–4183.
- (38) Ginzburg, V. V. Influence of Nanoparticles on Miscibility of Polymer Blends. A Simple Theory. *Macromolecules* **2005**, 38 (6), 2362–2367.

(39) Lipatov, Y. S.; Nesterov, A. E. Effect of Filler Concentration on the Phase Separation in Poly(Vinyl Acetate)-Poly(Methyl Methacrylate) Mixtures. *Polym. Eng. Sci.* **1992**, 32 (17), 1261–1263.

- (40) Du, M.; Wu, Q.; Zuo, M.; Zheng, Q. Filler Effects on the Phase Separation Behavior of Poly(Methyl Methacrylate)/Poly(Styrene-Co-Acrylonitrile) Binary Polymer Blends. *Eur. Polym. J.* **2013**, 49 (9), 2721–2729.
- (41) Thomas, E. L.; Talmon, Y. Selective Electron Beam Etching of Multicomponent Polymer Systems. *Polymer* **1978**, *19* (2), 225–227.
- (42) Han, C. C.; Bauer, B. J.; Clark, J. C.; Muroga, Y.; Matsushita, Y.; Okada, M.; Tran-cong, Q.; Chang, T.; Sanchez, I. C. Temperature, Composition and Molecular-Weight Dependence of the Binary Interaction Parameter of Polystyrene/Poly(Vinyl Methyl Ether) Blends. *Polymer* 1988, 29 (11), 2002–2014.
- (43) Lin, C.; Zuo, M.; Li, H.; Liu, T.; Zheng, Q. Morphology Evolution, Conductive and Viscoelastic Behaviors of Chemically Reduced Graphene Oxide Filled Poly(Methyl Methacrylate)/Poly-(Styrene-Co-Acrylonitrile) Nanocomposites during Annealing. *Chin. J. Polym. Sci.* 2015, 33 (8), 1162–1175.
- (44) Owens, D. K.; Wendt, R. C. Estimation of the Surface Free Energy of Polymers. J. Appl. Polym. Sci. 1969, 13 (8), 1741–1747.
- (45) Owens, D. K. Some Thermodynamic Aspects of Polymer Adhesion. J. Appl. Polym. Sci. 1970, 14 (7), 1725–1730.
- (46) Arganda-Carreras, I.; Kaynig, V.; Rueden, C.; Eliceiri, K. W.; Schindelin, J.; Cardona, A.; Sebastian Seung, H. Trainable Weka Segmentation: A Machine Learning Tool for Microscopy Pixel Classification. *Bioinformatics* **2017**, 33 (15), 2424–2426.
- (47) Lewis, J. P. Fast Normalized Cross-Correlation. *Vis. Interface* 1995, 120–123.
- (48) Haralick, R. M.; Shapiro, L. G. Computer and Robot Vision; Addison-Wesley Publ. Co.: 1992.
- (49) Hariharan, A.; Kumar, S. K.; Russell, T. P. Free Surfaces of Polymer Blends. II. Effects of Molecular Weight and Applications to Asymmetric Polymer Blends. *J. Chem. Phys.* **1993**, 99 (5), 4041–4050.
- (50) Lipatov, Y. Polymer Blends and Interpenetrating Polymer Networks at the Interface with Solids. *Prog. Polym. Sci.* **2002**, *27* (9), 1721–1801.
- (51) Duan, H.; Xie, E.; Han, L.; Xu, Z. Turning PMMA Nanofibers into Graphene Nanoribbons by In Situ Electron Beam Irradiation. *Adv. Mater.* **2008**, *20* (17), 3284–3288.
- (52) López-Barrón, C. R.; Macosko, C. W. Characterizing Interface Shape Evolution in Immiscible Polymer Blends via 3D Image Analysis. *Langmuir* **2009**, 25 (16), 9392–9404.
- (53) Hedegaard, A. T.; Gu, L.; Macosko, C. W. Effect of Extensional Viscosity on Cocontinuity of Immiscible Polymer Blends. *J. Rheol.* **2015**, 59 (6), 1397–1417.
- (54) Underwood, E. E. Quantitative Stereology; Addison-Wesley Publ. Co.: Reading, MA, 1970.
- (55) Lee, H. M.; Park, O. O. Rheology and Dynamics of Immiscible Polymer Blends. *J. Rheol.* **1994**, 38 (5), 1405–1425.
- (56) Veenstra, H.; Van Dam, J.; Posthuma De Boer, A. On the Coarsening of Co-Continuous Morphologies in Polymer Blends: Effect of Interfacial Tension, Viscosity and Physical Cross-Links. *Polymer* **2000**, *41* (8), 3037–3045.
- (57) Weon, B. M.; Won, K. H.; Macosko, C. W.; Je, J. H.; Seol, S. K.; Bell, J. R.; Pyun, A. Synchrotron X-Ray Microtomography for 3D Imaging of Polymer Blends. *Macromolecules* **2007**, 40 (6), 2029–2035.
- (58) López-Barrón, C. R.; Macosko, C. W. Direct Measurement of Interface Anisotropy of Bicontinuous Structures via 3D Image Analysis. *Langmuir* **2010**, *26* (17), 14284–14293.
- (59) Amaro-Gahete, J.; Benítez, A.; Otero, R.; Esquivel, D.; Jiménez-Sanchidrián, C.; Morales, J.; Caballero, Á.; Romero-Salguero, F. A Comparative Study of Particle Size Distribution of Graphene Nanosheets Synthesized by an Ultrasound-Assisted Method. *Nanomaterials* **2019**, 9 (2), 152.

Macromolecules

(60) López-Barrón, C. R.; Macosko, C. W. Rheological and Morphological Study of Cocontinuous Polymer Blends during Coarsening. *J. Rheol.* **2012**, *56* (6), 1315–1334.

- (61) López-Barrón, C. R.; Macosko, C. W. A New Model for the Coarsening of Cocontinuous Morphologies. *Soft Matter* **2010**, *6* (12), 2637.
- (62) Zhao, S.; Lou, D.; Zhan, P.; Li, G.; Dai, K.; Guo, J.; Zheng, G.; Liu, C.; Shen, C.; Guo, Z. Heating-Induced Negative Temperature Coefficient Effect in Conductive Graphene/Polymer Ternary Nanocomposites with a Segregated and Double-Percolated Structure. *J. Mater. Chem. C* 2017, 5 (32), 8233–8242.
- (63) Alig, I.; Pötschke, P.; Lellinger, D.; Skipa, T.; Pegel, S.; Kasaliwal, G. R.; Villmow, T. Establishment, Morphology and Properties of Carbon Nanotube Networks in Polymer Melts. *Polymer* **2012**, 53 (1), 4–28.